CTQ 327: A NEW GRAVITATIONAL LENS[1]

N. D. MORGAN,[2] M. D. GREGG,[3,4] L. WISOTZKI,[5] R. BECKER,[3,4] J. MAZA,[6] P. L. SCHECHTER,[7]
AND R. L. WHITE[8]

ABSTRACT

We present the second gravitationally lensed quasar discovered during the course of a *Hubble Space Telescope* Space Telescope Imaging Spectrograph snapshot survey for small-separation gravitational lenses. CTQ 327 is a double quasar with an image separation of $1\rlap.{''}22$ and a g-band flux ratio of roughly 5 to 1. Spectra reveal both components to be $z = 1.37$ quasars, and the lensing galaxy is clearly visible after point-spread function subtraction of the two quasar components. The light profile of the lensing galaxy is well modeled by an $r^{1/4}$ law, indicative of an early-type elliptical galaxy. An estimate of the lens galaxy redshift is $z \sim 0.4$–0.6, based on the Faber-Jackson relationship and photometric considerations, although values outside this range are still consistent with the present data. Resolved spectra of the two quasars show similar, but not identical, continuum and emission-line features: component A exhibits weaker emission lines with respect to the continuum than does component B, and there is evidence of intrinsic differences in the emission-line profiles between the two components. Optical monitoring of the quasar pair also shows a change in the g-band flux ratio of 0.14 mag over a 3 month period. These spectral and photometric differences may be due to microlensing fluctuations from stars in the lensing galaxy, intrinsic quasar variability coupled with the system's differential time delay, or some combination of the two. The observed variability makes CTQ 327 an attractive target for future flux monitoring, aimed at time-delay or microlensing studies.

Key words: gravitational lensing — quasars: individual (CTQ 327)

1. INTRODUCTION

Gravitationally lensed quasars have become an important tool for addressing a number of astrophysical questions. They have been used to study the mass function of intermediate-redshift galaxies (Kochanek et al. 2000), the bulge-to-disk mass ratio of spirals (Maller et al. 2000), and key cosmological parameters, such as the Hubble constant (Refsdal 1964) and statistical limits on the cosmological constant (Kochanek 1996). Systematic surveys at both radio (Browne et al. 2001; King et al. 1999; Winn 2001) and optical (Maoz et al. 1993; Wisotzki et al. 1996) wavelengths have replaced the often serendipitous discoveries of the past, bringing the number of confirmed lenses to well over 60.[9]

Here we present a new gravitationally lensed quasar discovered during the course of a *Hubble Space Telescope* (*HST*) snapshot survey for small-separation gravitational lenses. Our target quasars are selected primarily from the Calán-Tololo Survey (CTS; Maza et al. 1993), the FIRST Bright Quasar Survey (FBQS; White et al. 2000), and the Hamburg-ESO Quasar Survey (Wisotzki et al. 2000) and consist of bright ($B \lesssim 18.5$), high-redshift ($z \gtrsim 1$) quasars that have not been previously imaged at subarcsecond resolution. Direct CCD images were obtained with the Space Telescope Imaging Spectrograph (STIS; Kimble et al. 1997; Woodgate et al. 1998) and consist of three dithered exposures taken through the 50 CCD clear (CL) aperture and a single long-pass exposure taken through the F28X50LP (LP) filter. The exposure times are scaled according to the target's brightness, but are typically between 1 and 2 minutes at each dither position. The advantage of using *HST* to search for gravitational lenses is its superior angular resolution; the separation between lensed images scales as the square root of the deflecting mass, which makes it difficult to probe the small end of the lens mass spectrum from the ground. From theoretical considerations, roughly 40% of gravitational lenses arising from intervening elliptical galaxies, and 70% from spiral galaxies, are expected to have image separations smaller than $1''$, with nearly half of all spiral lenses having image separation smaller than $0\rlap.{''}5$ (Fukugita et al. 1992). These small-separation systems are easily accessible only with *HST*.

During Cycle 8 imaging, we obtained STIS snapshots of 154 quasars and have discovered two new gravitational lenses. The first, HE 0512−3329, is a $0\rlap.{''}64$ double drawn from the Hamburg-ESO survey and is likely lensed by a spiral galaxy. It is described in detail by Gregg et al. (2000). The second, and the topic of this paper, is the $1\rlap.{''}22$ double CTQ 327. We describe the discovery of the system and follow-up spectroscopy, IR imaging, and optical imaging in

[2] Center for Astronomy and Astrophysics, Yale University, New Haven CT 06520; nicholas.morgan@yale.edu.

[3] Physics Department, University of California at Davis, 1 Shields Avenue, Davis, CA 95616.

[4] Institute for Geophysics and Planetary Physics, Lawrence Livermore National Laboratory, University of California, 7000 East Avenue, Livermore, CA 94550; bob@igpp.llnl.gov, gregg@igpp.llnl.gov.

[5] Astrophysical Institute Potsdam, An der Sternwarte 16, D-14482 Potsdam, Germany; lutz@aip.de.

[6] Departamento de Astronomía, Universidad de Chile, Casilla 36-D, Santiago, Chile; jmaza@das.uchile.cl.

[7] Department of Physics, Massachusetts Institute of Technology, 77 Massachusetts Avenue, Cambridge MA 02139; schech@space.mit.edu.

[8] Space Telescope Science Institute, 3700 San Martin Drive, Baltimore, MD 21218; rlw@stsci.edu.

[9] See the CfA-Arizona Space Telescope Lens Survey (CASTLES) at http://cfa-www.harvard.edu/castles.

§ 2. These observations leave no doubt that CTQ 327 is gravitationally lensed, and in § 3 we present our results from preliminary optical monitoring of the twin quasar images. We assess the quasar variability observed to date, discuss the nature and probable redshift of the lensing galaxy, and present a lens model and time delay estimate for the system in § 4. We summarize our findings in §5.

2. INITIAL OBSERVATIONS AND ANALYSIS

2.1. *Background and HST STIS Observations*

The object CTQ 327 ($13^h55^m43^s.44$, $-22°57'23''.0$; J2000.0) was first identified as a $B = 18.2$ quasar from the fifth installment of the Calán-Tololo Survey (Maza et al. 1993) and was independently discovered as part of the Hamburg-ESO Quasar Survey (HE 1352−2242). The CTS is a wide-field objective-prism survey aimed at discovering quasars and emission-line galaxies in the southern sky. The survey has been successful in discovering double quasars as well, yielding two other gravitational lenses (CTQ 286: Claeskens, Surdej, & Remy 1996; CTQ 414: Morgan et al. 1999). The CTS originally quoted a tentative redshift for CTQ 327 of $z \sim 2$, based on the identification of a single emission line in the objective-prism spectra, which was presumed to be Lyα. Follow-up spectral observations have placed the quasar's redshift at $z = 1.37$, so that the correct identification for the CTS feature was actually C IV.

The STIS snapshot sequence for CTQ 327 was obtained on 1999 August 3 and consisted of three 60 s dithered exposures taken through the CL aperture and one additional 120 s exposure taken through the LP filter. All observations were taken with a gain setting of 4 e^- ADU^{-1} and a corresponding CCD read noise of 7 e^-; the STIS detector scale is $0''.0508$ pixel^{-1}. Each observation was divided into two CR-split exposures to facilitate cosmic ray removal. The response function of the CL aperture is essentially defined by the telescope throughput and spectral sensitivity of the STIS CCD and has an effective wavelength and FWHM of 6168 and 4410 Å, respectively. The LP bandpass has a spectral response similar to that of the CL aperture redward of 5500 Å (Gregg & Minniti 1997), with an effective wavelength and FWHM of 7333 and 2721 Å, respectively. A drizzled image (Fruchter & Hook 1997) of the three CL exposures is shown in Figure 1. The separation between components A (brighter) and B (fainter) is $1''.224$, based on Gaussian fits to the profile cores. Using component A as a point-spread function (PSF) template, we find an average magnitude difference between the two components of 1.88 mag in the CL exposure and 1.75 mag in the LP exposure. The similarity in the CL and LP flux ratios provided the initial evidence that both components might be similarly redshifted quasars, rather than a chance alignment of a quasar with a foreground Galactic star.

2.2. *Spectral Observations*

To determine the exact nature of the two components, we obtained spectra of CTQ 327 A and B with the Echelle Spectrograph and Imager (ESI; Epps & Miller 1998) at the Keck Observatory on 2000 April 6. The 500 s observation was taken in low-dispersion mode, which provided a useful wavelength coverage of 3800–9600 Å and a wavelength scale that varied roughly linearly from 0.7 Å pixel^{-1} at 3800 Å to 9 Å pixel^{-1} at 9600 Å. We used a 1″ slit oriented
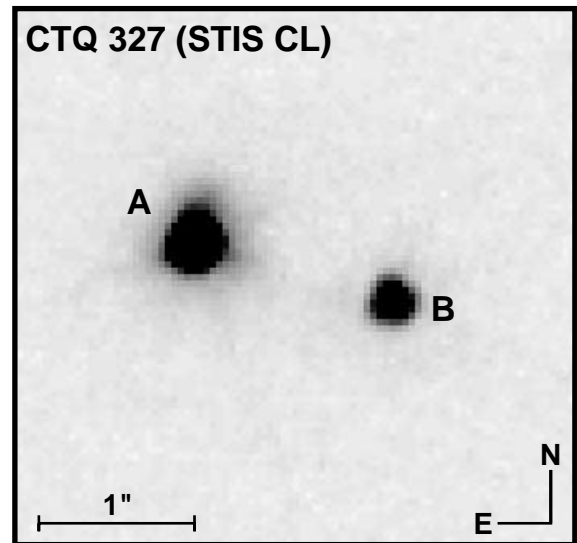

FIG. 1.—Drizzled image of three 60 s exposures of CTQ 327 A and B taken with *HST* STIS. The image has been reconstructed using a scale of $0''.0375$ pixel^{-1}.

along the line connecting the two quasars, corresponding to a position angle of 252° east of north, such that both spectra could be extracted from the same frame.

Since the seeing during the ESI observation ($0''.8$ FWHM) was more than half the image separation, some overlap between the two spectra was unavoidable, and the spectra had to be decomposed from each other to leave as little mutual interference as possible. This was accomplished by an iterative fitting routine, modeling the components as two overlapping Moffat profiles of fixed separation and identical width. In repeated passes, the centroid and the profile width were first determined as functions of wavelength; these were then represented by low-order polynomials and held fixed in subsequent passes, until finally only the two profile amplitudes remained to be fitted. The residual image after subtracting the fitted model revealed some asymmetries in the PSF, but the overall fit quality was quite good, as indicated by the reduced χ^2 of 0.86.

The position angle of the two images of CTQ 327 was far from the parallactic angle during the ESI observation, obtained at an air mass of 1.45, resulting in very poor flux calibration. To correct this, we observed CTQ 327 and a nearby spectrophotometric standard on 2000 May 3 at Lick Observatory, using the Kast Double Spectrograph with a $1''.5$ wide slit set to the parallactic angle; the air mass was 1.73. The 2″ seeing made it impossible to resolve the two components, but assured that light from both images was well-mixed in the slit. The Kast spectrum, covering 3400–8200 Å, provides the correct flux for the sum of the components, while the resolved ESI spectra are assumed to provide the correct relative fluxes, enabling us to obtain the correct flux calibration of each. The extracted, flux-calibrated spectra of the two components are shown in the top panel of Figure 2.

Both spectra are consistent with similarly redshifted quasars. The emission properties for the two components are summarized in Table 1. Gaussian fits to the peaks of the C III] profiles give an average redshift of $z = 1.366$, while a slightly higher redshift of $z = 1.373$ is found using the Mg II
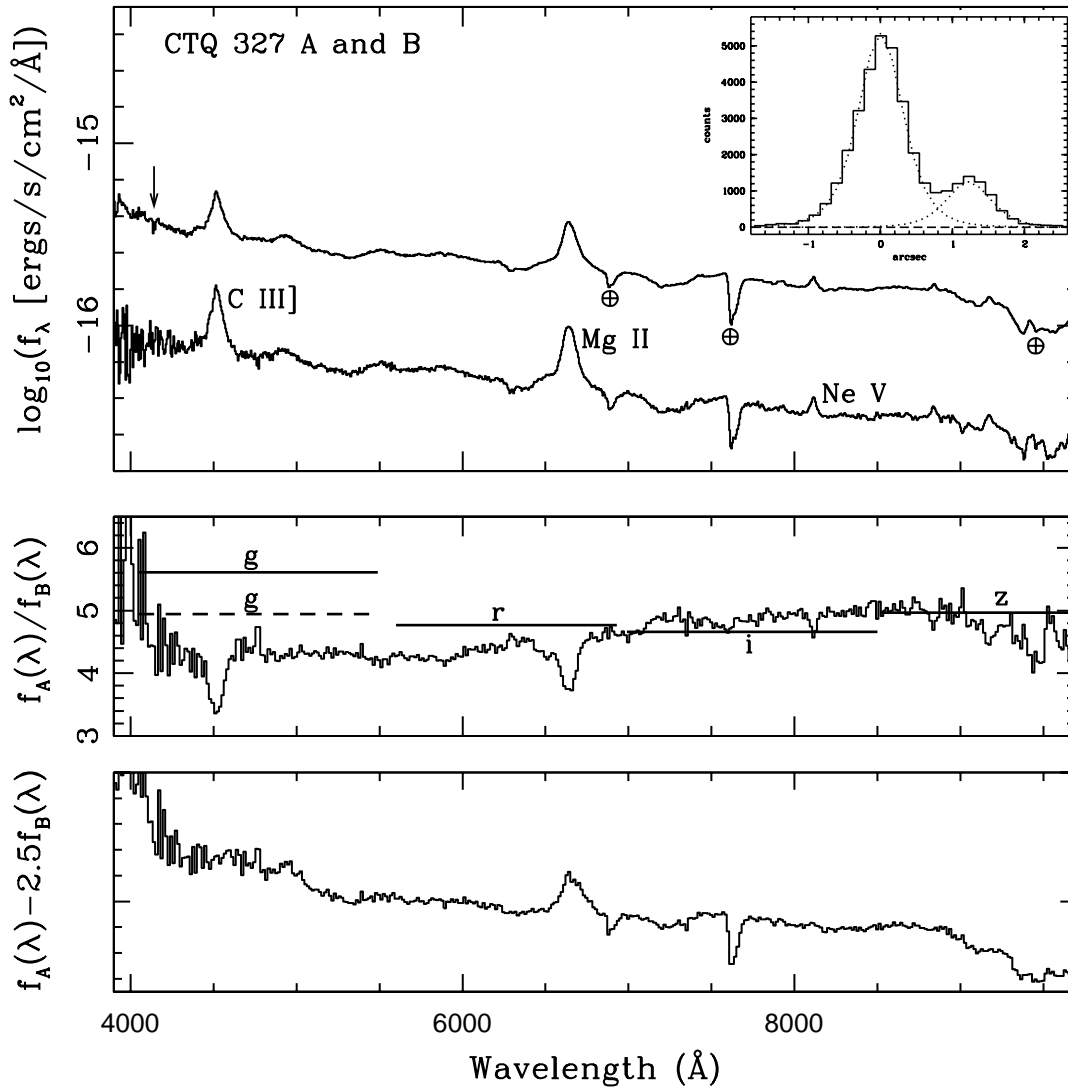
FIG. 2.—*Top*: Keck ESI spectra of CTQ 327 A and B taken 2000 April, binned at a resolution of 6 Å. The inset (*top right*) is a cut perpendicular to the spectra, showing that both components are resolved. The arrow at 4140 Å marks the location of a weak Mg II absorption doublet present in the spectrum of the brighter component. *Middle*: Ratio of component A to B. Shown are the *griz* flux ratios from Magellan observations from 2001 March (*solid horizontal lines*) and the *g* flux ratio from 2001 June (*dashed line*). *Bottom*: Difference spectrum after scaling B by 2.5 and subtracting from A.

profiles. The spectra are also fairly clean of intervening absorption, with the possible exception of a weak Mg II $\lambda\lambda2796, 2803$ absorption doublet (Fig. 2, *arrow*) seen in component A's spectrum at around 4140 Å. The rest-frame equivalent width is ~0.5 Å for each component of the dou-

blet. If its identification is correct, then the implied absorber redshift is $z = 0.48$.

While the spectra of the two components are similar, they are not identical. The quotient of the two spectra (Fig. 2, *middle*) shows that the A/B continuum ratio increases from 4.37 at 4500 Å to 5.03 at 8500 Å. Component A also has weaker emission lines relative to the continuum level than does component B, as seen by the dips in the spectral ratio at the locations of C III], Mg II, and Ne V. These differences can be explained by adding a relatively soft continuum component to A's spectrum. However, the ratio of equivalent widths for the emission lines (see Table 1) decreases from 0.72 for Mg II to 0.56 for C III]. If this difference were solely due to enhanced continuum emission in component A's spectrum, then the ratio of continuum levels at these wavelengths would change by the same factor, but this is not observed. The A/B continuum ratio changes from 4.53 under Mg II to 4.37 under C III], a drop by a factor of 1.04, while the equivalent width ratios drop by a factor of 1.28 between the same two features. This is demonstrated in the

TABLE 1
REDSHIFT ANALYSIS FOR CTQ 327 A AND B

Profile	Component	λ_{obs}	λ_{rest}	z	EW (Å)
C III].........	A	4515.4	1908.7	1.3656(3)	25.5
C III].........	B	4515.6	1908.7	1.3658(6)	45.2
Mg II	A	6640.0	2798.1	1.3731(1)	45.7
Mg II	B	6640.6	2798.1	1.3733(1)	63.5

NOTES.—Numbers in parentheses are 1 σ errors. Equivalent widths are reported in the quasar rest frame.

bottom panel of Figure 2, where we show the difference in the two spectra after scaling component B's spectrum by a factor of 2.5. The subtracted spectrum is relatively clean at the location of C III], but a significant positive residual is present at the location of Mg II. Similarly, scaling component B's spectrum such that Mg II subtracts out smoothly leaves a significant negative residual at the location of C III]. This cannot be explained solely by rescaling the continuum emission in one of the components and argues for intrinsic differences in the shapes of the emission-line profiles between the two quasar images.

2.3. Detection of the Lensing Galaxy

2.3.1. Keck NIRC Observations

To search for direct signs of a lensing galaxy, we obtained K-band images of CTQ 327 using the Near Infrared Camera (NIRC; Matthews & Soifer 1994) on the Keck telescope on 2000 April 18. Six 120 s dithered images were obtained through typical seeing of 0″.5 FWHM. The frames were bias subtracted and flat-field corrected using standard IRAF tasks.

The stacked image of the double quasar is shown in Figure 3a. We have resampled the stacked image using the IRAF task MAGNIFY to a scale of 0″.0478 pixel^{-1}, roughly a factor of 3 larger than the raw data, which reduces aliasing patterns that appear during PSF subtraction. A PSF template was constructed from a bright nearby star that

appeared on three of the six dithered images. The residual pattern after fitting a two-component PSF model with the IRAF DAOPHOT package is shown in Figure 3b.

The residual pattern shows clear signs of unmodeled flux between the two quasar components, showing a swath of positive residuals between the two components with a peak of $+15 \sigma$ (where σ is the rms sky noise of the resampled image). A natural explanation is that we are seeing flux from the unmodeled lensing galaxy. We next fit a three-component model consisting of two PSFs and a circularly symmetric $r^{1/4}$ profile, convolved with the PSF template, to model the galaxy flux. The relative positions and flux ratios of the three components, as well as the effective radius of the galaxy profile, were treated as free parameters. A least-squares fit to the stacked image was then performed within IDL, using a downhill-simplex algorithm for the minimization (Press et al. 1992). The residual pattern after the three-component fit is shown in Figure 3c and is much cleaner than for the two-PSF model. There is no extended structure seen above the 3 σ level, indicating that the diffuse source of flux is well described by the $r^{1/4}$ profile. The unsubtracted galaxy flux for the three-component model is shown in Figure 3d.

The optimized model places the centroid of the galaxy (G) closer to the fainter B image ($\theta_{BG} = 0″.32$) than the brighter A image ($\theta_{AG} = 0″.90$), with the galaxy displaced slightly to the southeast by 0″.07 with respect to the AB line. The AB separation is 1″.207, slightly smaller than the *HST* STIS separation of 1″.224, but consistent with a 2% change
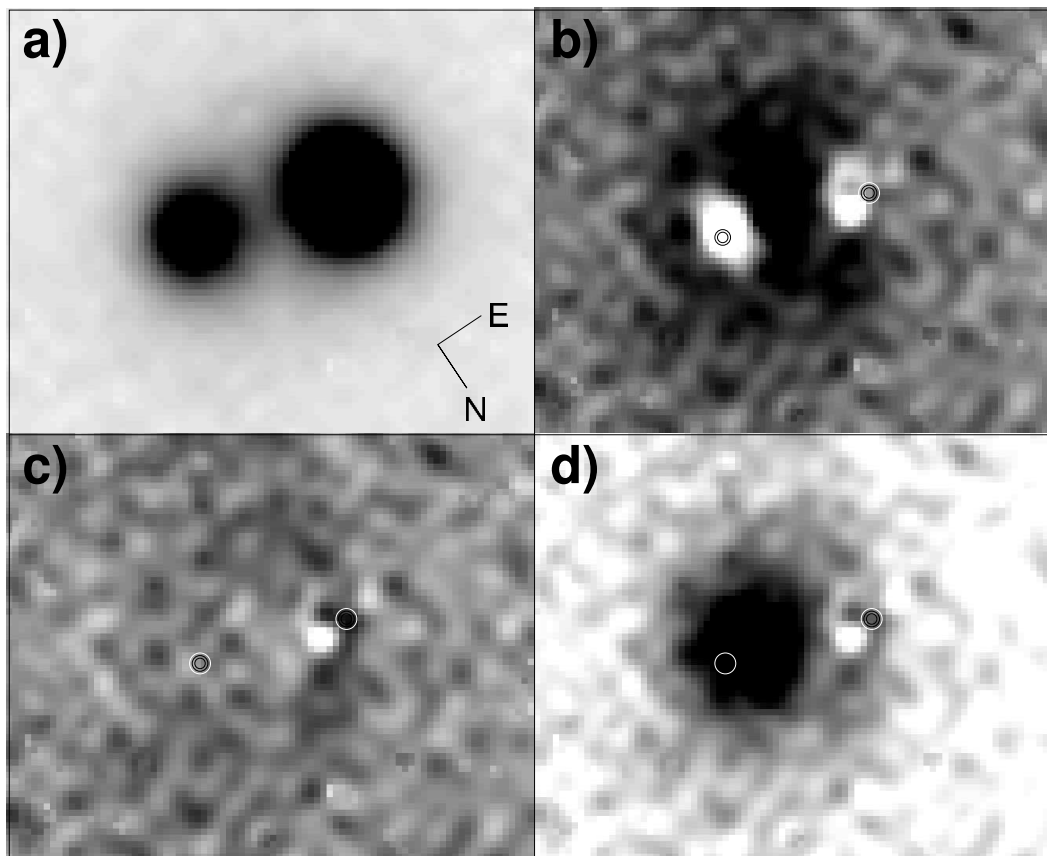

FIG. 3.—(a) Stacked K-band image of CTQ 327 obtained with NIRC on Keck, resampled at a scale of 0″.0478 pixel^{-1}. (b) Residuals of (a) using a two-component PSF model. (c) Residuals of (a) using a three-component model consisting of two PSFs and a circularly symmetric $r^{1/4}$ profile (convolved with the PSF template). (d) The same as (c), but with the two PSFs subtracted and the galaxy left in place. The saturation levels for (b) and (c) are at $\pm 7 \sigma$, where σ is the rms sky noise of the resampled image. The contrast for panels (a) and (d) have been scaled to the brightness of the quasar and galaxy.

in the nominal NIRC plate scale. The best-fit effective radius of the lensing galaxy is $1\farcs4$, and the A/B flux ratio for the fit is 3.55. These results agree well with a simple singular iso-thermal sphere (SIS) potential model for the lensing galaxy and leave little doubt that the system is lensed. The SIS model assumes a circularly symmetric lensing potential and predicts an θ_{AG}/θ_{BG} separation ratio equal to the A/B flux ratio, with the fainter quasar image located closer to the lensing galaxy, as seen with CTQ 327. The ratio of quasar-galaxy distances (2.8) is about 25% smaller than that expected from the observed flux ratio, which we regard as a good agreement given the simplicity of the model.

The K-band galaxy magnitude has been estimated from aperture photometry on the unsubtracted galaxy profile, that is, in Figure 3d. We have used an aperture diameter of twice the galaxy's effective radius and have flux calibrated the data using standard star observations taken during the April Keck run. This gives a magnitude of $K = 16.8$ and includes a fiducial 0.75 mag aperture correction to compen-sate for half of the flux expected to lie outside of 1 effective radius. Aperture photometry for the two quasar images was performed on the reconstructed model without the galaxy, using an aperture radius of $0\farcs5$, an aperture correction of 0.29 mag, and yield magnitudes of $K = 15.88$ and $K = 17.19$ for components A and B, respectively.

2.3.2. *HST WFPC2 Observations*

To get a better handle on the astrometric and photometric properties of the lensing galaxy, CTQ 327 was reobserved with *HST* as part of Cycle 10 of CASTLES (PI: E. E. Falco) on 2001 May 24. A total of 12 exposures were taken using the Wide Field Planetary Camera 2 (WFPC2), six each through the F555W and F814W bandpasses (hereafter V and I, respectively). Integration times were either 200 or 260 s for each exposure. The cleaned images may be viewed online at the CASTLES Web site.

To separate the lens and source components, we have fitted and subtracted PSF models to the stacked and cosmic-ray–removed V- and I-band frames. For the brighter quasar com-ponent, our PSF was generated using the Tiny Tim package (ver. 6.0; Krist & Hook 1997)[10] using the appropriate bandpasses and chip positions, while for the fainter quasar component, the PSF was taken to be an excised subraster of the stacked frame centered on the brighter quasar component itself. The latter approach does a better job of modeling the core of the PSF, which is important for the fainter compo-nent, given its proximity to the lensing galaxy. After PSF sub-traction, residuals at the center of components A and B were $\sim$6% and $\sim$4% of the respective peaks.

The lensing galaxy was confidently detected in the I-band–subtracted image, but only marginally detected in the V-band–subtracted image; below we report results only from the I-band data. The relative astrometry for the system, as determined from Gaussian fits to the cores of components A and B and to the galaxy center after PSF subtraction, is presented in Table 2. The three components are slightly mis-aligned in a manner similar to the K-band configuration, with the galaxy center offset by $0\farcs042$, approximately to the south-east with respect to the quasar line. The quasar AB separation is $1\farcs224$ and agrees with the separation determined from the STIS discovery observations.

---

[10] See http://www.stsci.edu/software/tinytim.

TABLE 2
HST F814W ASTROMETRY

Object	Δ R.A. (arcsec)	Δ Decl. (arcsec)
A	$\equiv 0$	$\equiv 0$
B	-1.1734	-0.3477
G	-0.8774	-0.3037

To estimate the galaxy magnitude, we measured flux within a small 5 pixel ($0\farcs23$) radius aperture, within which galaxy flux is clearly discernible from sky background and residual PSF contamination from components A and B should be close to negligible. We use a WFPC2 zero-point correction of 21.64 mag (Holtzman et al 1995). This gives a galaxy magnitude of $I = 22.6$, and is certainly a lower limit to the total galaxy magnitude. For the sake of computing galaxy colors, we have determined an aperture correction of -1.8 mag from an aperture radius of $0\farcs5$ to the K-band effective radius of $1\farcs4$, as determined from a synthetic $r^{1/4}$ profile (with $R_{\rm eff} = 1\farcs4$) convolved with the WFPC2 PSF. This gives an estimate for the I-band galaxy magnitude inside 1 K-band effective radius of $I = 20.8$.

3. FOLLOW-UP OPTICAL OBSERVATIONS

We have begun optical monitoring of the quasar images using the Magellan Consortium's 6.5 m Walter Baade Telescope at the Las Campanas Observatory (LCO). Our purpose is to assess the amplitude and frequency of variabil-ity associated with the two quasar components. The ultimate goal is to determine if CTQ 327 will be useful for measuring H_0 from the system's differential time delay (Refsdal 1964) or for microlensing studies of the lensing gal-axy and source quasar (Witt, Mao, & Schechter 1995). In the following section, we present our first- and second-epoch data for the quasar pair, describe our photometric solutions intended to calibrate future observations, and discuss the degree of variability observed for the two quasar images thus far.

3.1. *First-Epoch Data*

First-epoch optical images of CTQ 327 A and B were obtained on the nights of 2001 March 24 and 25. Direct images were taken using the Magellan Instant Camera (MagIC) CCD, which houses an SITe 2048×2048 pixel array with a scale of $0\farcs0692$ pixel^{-1}. The average gain for this four-amplifier detector is $1.96\ e^-$ DN^{-1} with a read noise of $5.25\ e^-$. The telescope uses an active optics design, employing a Shack-Hartman wavefront sensor to compen-sate for aberrations in the primary mirror. The observing conditions were photometric for both nights, with a seeing FWHM that ranged between $0\farcs6$ and $0\farcs7$. We show a $2\farcm4 \times 2\farcm4$ field of view of CTQ 327 and surroundings in Figure 4. The Galactic latitude for this field is somewhat high ($b = 38°$), which limits the number of comparably bright stars that can be used as PSF templates.

Observations of CTQ 327 were taken through a comple-ment of Sloan Digital Sky Survey (SDSS; York et al. 2000) *griz* filters. Exposure times were either 360 or 720 s, with dithered offsets of several arcseconds between each exposure. The raw images were bias subtracted, flat-field
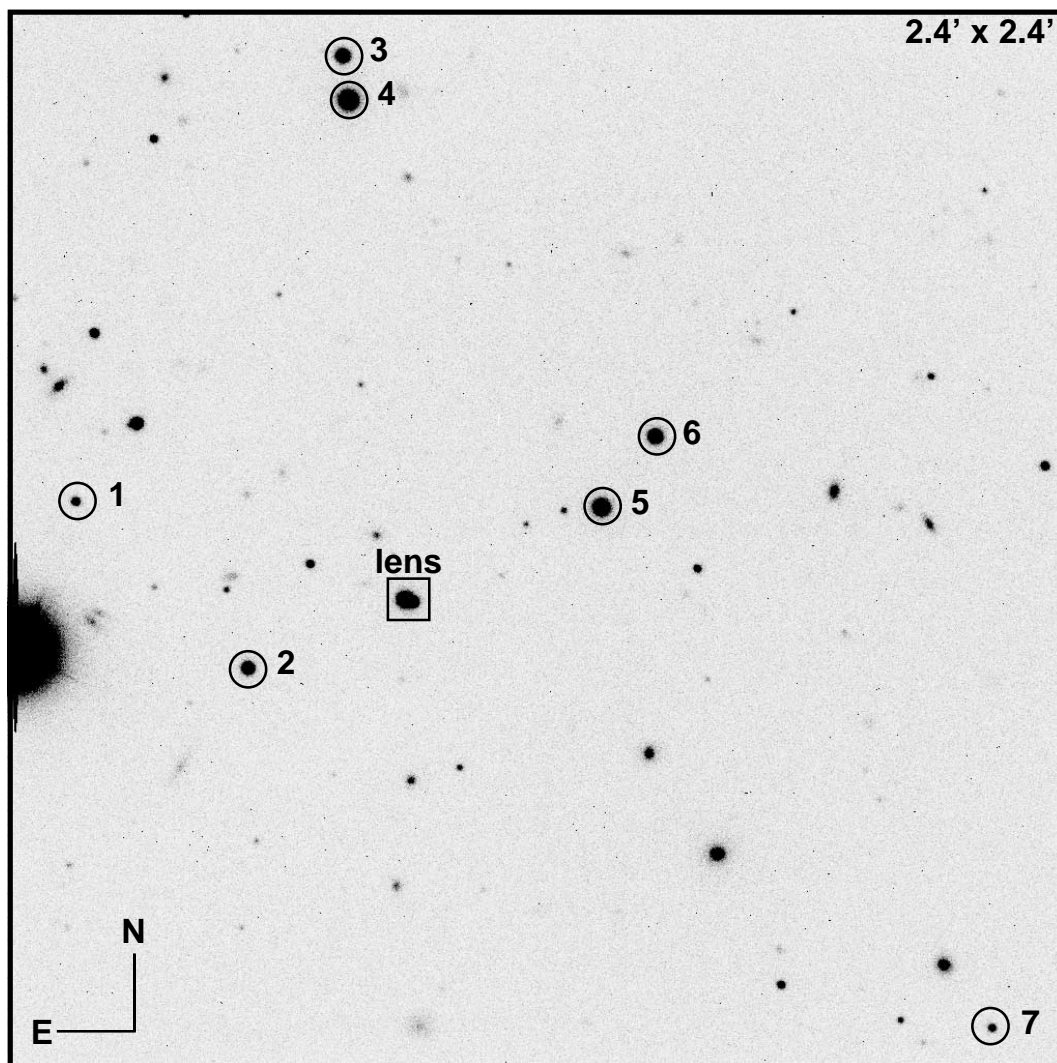
Fig. 4.—A $2'.4 \times 2'.4$, 360 s *i*-band exposure of CTQ 327 (*box*) and surroundings, obtained with the Magellan 6.5 m telescope. Photometry and relative astrometry for the seven circled field stars are reported in Table 3.

corrected, and trimmed using the VISTA program, and the *z*-band data were fringe corrected by subtracting off an appropriately scaled fringe template.

At first, we fitted a two-component PSF model to the double quasar, to judge the degree of galaxy contamination in each of the four filters. Only star 5 in Figure 4 was usable as a PSF, the other stars being either too close to the detector edge to construct PSF subrasters or simply too faint to give an adequate signal-to-noise ratio to model the blue quasar light in *g*. Star 2, which was used as the *K*-band PSF, falls into the latter category. Each frame was fitted separately, and the residuals were then stacked to look for excess galaxy light in the two-component fit.

No indication of unaccounted flux was found in the stacked *g* and *r* frames, but a pattern similar to that in Figure 3*b*, at a level of 5–10 times the rms sky noise, did emerge in the stacked *i* and *z* frames. A third component was added to the *i* and *z* models, which we again took to be a circularly symmetric $r^{1/4}$ profile convolved with the PSF template. The galaxy's effective radius and relative position are poorly constrained by the Magellan data, so we have fixed both quantities using results from the Keck NIRC observations

and solved for the fluxes of the three components and the relative position of component B with respect to A. Our results are presented in Table 3. The A/B flux ratio for the pair shows a small increase with wavelength across the *r*, *i*, and *z* filters (4.66, 4.76, and 4.87, respectively) and a 20% larger value through the *g* filter (5.61). The galaxy magnitude showed considerable scatter in *i* (rms of $\sim$1 mag) and *z* (rms of 0.3 mag), and we report only the *z*-band magnitude in Table 3. The galaxy magnitude has been obtained from aperture photometry performed on the convolved $r^{1/4}$ profile, again with a fiducial 0.75 mag aperture correction.

3.2. *Photometric Calibration*

The photometric zero points and color terms for the Magellan data were derived using observations of the Landolt standard stars Rubin 152E and 152F, 107-614, and GD 108, and the Oke standard star G60-54. Standard Johnson-Kron-Cousins magnitudes were adopted from Landolt (1992) for the Landolt standards and from Bessel (1990) for the Oke standard. These magnitudes were then placed onto the SDSS system using the synthetic transformations given by Fukugita et al. (1996). Since our standard observations

TABLE 3
Magellan Photometry and Astrometry for CTQ 327 and Field

Object	g	r	i	z	ΔR.A. (arcsec)	ΔDecl. (arcsec)
A......................	17.707(1)	17.322(1)	17.338(3)	17.427(7)	$\equiv 0$	$\equiv 0$
B......................	19.580(4)	18.994(4)	19.032(22)	19.145(21)	-1.1740	-0.3470
G	...	...	...	21.9(3)	$\equiv -0.8295$	$\equiv -0.3444$
1......................	21.173(9)	20.218(4)	19.917(11)	19.848(43)	43.9	13.2
2......................	20.561(3)	19.307(3)	18.180(3)	17.694(6)	21.0	-9.1
3......................	20.386(4)	19.040(2)	17.842(5)	17.313(3)	7.8	72.8
4......................	17.190(3)	16.632(12)	16.488(9)	16.487(21)	7.1	66.8
5......................	17.883	17.233	17.066	17.047	-26.4	12.2
6......................	18.257(2)	17.791(3)	17.692(2)	17.723(5)	-33.7	21.7
7......................	20.890(13)	20.413(8)	20.309(4)	20.398(26)	-78.2	-57.6

Notes.—Errors are 1 σ dispersions from PSF fitting and do not include uncertainties in the PSF star's magnitude or systematic errors associated with the photometric calibration. The PSF star 5 has g, r, i, and z aperture photometry uncertainties of 0.023, 0.023, 0.011, and 0.040 mag, respectively. Photometry is reported for the 2001 March observations. Object numbers correspond to the labels in Fig. 4.

did not span a large air-mass range, they cannot be used to derive extinction coefficients, as the results would be degenerate with the photometric zero points. We have therefore adopted extinction coefficients of $k_g = 0.17$, $k_r = 0.09$, $k_i = 0.03$, and $k_z = 0.03$, taken from the photometry catalog of Newberg et al. (1999), and have solved for zero points and $g-r$ color terms. The photometric solutions for each filter are presented in Table 4.

Since the goal is to provide a local set of standards that can be used to calibrate future observations of the quasar images, we have placed the PSF star 5 onto the standard system using the above transformations, but have derived only relative photometry (from PSF fitting) with respect to star 5 for six other stars in the field. The relative photometry and astrometry for the local standards are presented in Table 3.

3.3. Second-Epoch Data

We obtained second-epoch Magellan data on 2001 June 13 using the same instrument described above. The observing conditions for the night were marred by intermittent cirrus, and the Shack-Hartman sensor was not activated during the CTQ 327 observations, which contributed to a PSF with a larger FWHM (1″2) than for the March run. Three 120 s exposures were taken through the g-band and were reduced using procedures identical to those described above. Results from a two-component PSF fit give g-band magnitudes of 17.832 ± 0.001 and 19.568 ± 0.013 for components A and B, where the values have been calibrated using the March local standards. Comparing the March and

TABLE 4
Photometric Solutions for the March Magellan Run

Filter	c_1	c_2	σ (mag)
g......................	26.647	0.048	0.019
r......................	26.976	-0.061	0.038
i......................	26.529	-0.023	0.052
z......................	25.372	0.035	0.060

Note.—The σ-values denote the rms dispersion in the calibration.

June data, component A has dimmed by 0.125 ± 0.001 mag, while component B shows a negligible brightening of 0.012 ± 0.014 mag. The change in the magnitude difference between the two components, as computed solely from the PSF flux ratios, is 0.137 ± 0.014 mag. This latter measurement is independent of the calibration scheme used to determine the separate quasar magnitudes and therefore is free from any systematic errors that may be present in the calibration of the June data. Thus, there is evidence for $\gtrsim 10\%$ variability between the two quasar images over a 3 month period.

4. DISCUSSION

4.1. Variability Assessment

The g-band Magellan observations show a variation in the A/B flux ratio of the two quasars of 0.14 mag over a period of 3 months. We can get a handle on variability over a longer baseline by comparing with the spectra from 2000 April. Figure 2 (*middle*) shows the quotient spectrum for the two components, along with the *griz* flux ratios from the March run (*solid horizontal lines*) and the g flux ratio from the June run (*dashed horizontal line*). The broadband i and z flux ratios agree to within ~ 0.05 mag with the corresponding spectral values, but larger differences are observed toward bluer wavelengths. The r-band ratio differs from the spectral ratio by ~ 0.1 mag, the June g-band ratio by ~ 0.15 mag, and the March g-band ratio by ~ 0.3 mag.

The temporal variation in the g-band flux ratios may be a result of intrinsic variability of the source quasar, microlensing fluctuations from stars in the lensing galaxy, or some combination of the two. There are two lines of evidence that suggest microlensing may be present. First, as discussed in § 2.2, the A/B spectral continuum ratio increases from 4.37 at 4500 Å to 5.03 at 8500 Å. Such an increase is clearly not due to contamination of component B's spectrum by galaxy light, since one would then expect the A/B continuum ratio to decrease toward redder wavelengths. Also, contamination of component A's spectrum by galaxy light seems unlikely, since A is further from the lensing galaxy than B. The variation is consistent with enhanced continuum emission from component A, possibly from microlensing of A's continuum by stars in the lensing galaxy. Such a

wavelength-dependent magnification is consistent with theoretical predictions of microlensing by stars in a foreground lensing galaxy (Kayser, Refsdal, & Sabell 1986) and has been seen (on a stronger level) in other lensed quasars that are known to be microlensed (e.g., HE 1104−1805; Wisotzki et al. 1993). Second, the changes in the broadband flux ratios are more pronounced toward the blue, as one might expect if they were due to microlensing. The red emission region of quasar accretion disks should be less efficiently microlensed than the more compact blue emission region, since the larger source size tends to average over small-scale structure present in microlensing caustic patterns. Thus, we conclude that there is some evidence for microlensing-induced variations.

The reasoning above also suggests that the emission lines of quasars, which are thought to arise from a region an order of magnitude larger than the continuum emission, should be relatively unaffected by microlensing. The same argument therefore cannot account for the differences in emission profiles observed for the two components (Fig. 2, *bottom*). Instead, these differences may be the result of intrinsic variability of the quasar's broad-line region combined with the differential time delay between the images or the result of a more complicated microlensing pattern that affects both the continuum and broad-line regions of the source quasar. Broadband and spectral monitoring of the two components over a longer baseline are needed to determine which mechanisms are responsible for the observed variability.

4.2. *Nature of the Lensing Galaxy*

The lensing galaxy is likely an early-type elliptical based on the $r^{1/4}$ light profile and the lack of strong absorption features in the quasar spectra. While it is tempting to associate the weak Mg II absorption doublet at $z = 0.48$ with the lensing galaxy, the argument is not very persuasive, as one generally expects to find a Mg II absorption feature in the spectra of $z \sim 1$ unlensed quasars as well (Steidel & Sargent 1991). We can statistically estimate the lens redshift from the lens-redshift probability distribution of Kochanek (1992). Using the quasar redshift and image separation as constraints, we find a most probable lens redshift of $z = 0.55$ with a 1 σ probability interval of $0.33 < z < 0.74$. [Throughout this section, we adopt a flat $(\Omega_m, \Omega_\Lambda) = (0.3, 0.7)$ cosmology and parameterize the Hubble constant by $H_0 = 100\, h\, \mathrm{km\, s^{-1}\, Mpc^{-1}}$.]

The 1″.22 image separation is a direct measure of the depth of the galaxy potential. Adopting a simple SIS model for the lensing potential and a lens redshift of 0.55, then the predicted line-of-sight velocity dispersion for the lensing galaxy is 200 km s^{-1}. This corresponds to a mass within the system's Einstein radius (a linear size of 2.7 h^{-1} kpc at $z = 0.55$) of $5.0 \times 10^{10}\, h^{-1}\, M_\odot$.

We can add an additional constraint on the lens redshift by using the fact that the lensing galaxy's velocity dispersion (as estimated from the observed image separation) is related to the galaxy's brightness as a function of redshift. By using the galaxy photometry from § 2, the redshift of the lensing galaxy can be constrained. For this analysis, we assume the galaxy's central velocity dispersion is related to its B-band luminosity L via a Faber-Jackson relationship (Faber & Jackson 1976) of the form $L/L_* = (\sigma/\sigma_*)^\gamma$, where L_* corresponds to a B-band magnitude of $M_* = -19.7 + 5\log h$,

and we adopt $\sigma_* = 220$ km s^{-1} and $\gamma = 4.0$ for early-type galaxies. For a given redshift z, we can then estimate the cosmological distance modulus of the lensing galaxy from

$$m_{\mathrm{AB}}(\lambda_{\mathrm{obs}}) - M_{\mathrm{AB}}(\lambda_{\mathrm{rest}}) = 5\log\left(\frac{D_L}{10\ \mathrm{pc}}\right) + 7.5\log(1+z)\,,$$
(1)

where D_L is the angular diameter distance to the lens. For calculating $M_{\mathrm{AB}}(\lambda_{\mathrm{rest}})$, a spectral energy distribution (SED) for an early-type galaxy was obtained from S. Lilly (1997, private communication), which consisted of interpolated and extrapolated values of the SEDs presented by Coleman, Wu, & Weedman (1980). The SED is then normalized to the Faber-Jackson luminosity at $4400(1 + z)$ Å, which yields the predicted AB magnitudes. To transform back to standard magnitudes, we use $I = I_{\mathrm{AB}} - 0.456$ (Fukugita, Shimasaku, & Ichikawa 1995) and $K = K_{\mathrm{AB}} - 1.86$ (Allen & Cox 2000).

Figure 5 shows the predicted K-band magnitude versus $I-K$ color of the lensing galaxy (*heavy solid line*) as a function of the unknown galaxy redshift, as constrained by the quasar source redshift and the observed image separation. The thin solid lines above and below this curve are the expected 1 σ error in the predicted K-band magnitude from the observed scatter in the Faber-Jackson relationship (Dressler et al. 1987). The lensing galaxy appears systematically redder as it is placed at higher redshifts. The observed K-band magnitude of the lens ($K = 16.8$) is marked by the dashed horizontal line.

As can be seen from the figure, the galaxy's observed K-band magnitude is degenerate over much of the redshift range and yields only a wide constraint of $0.23 < z < 1.14$,
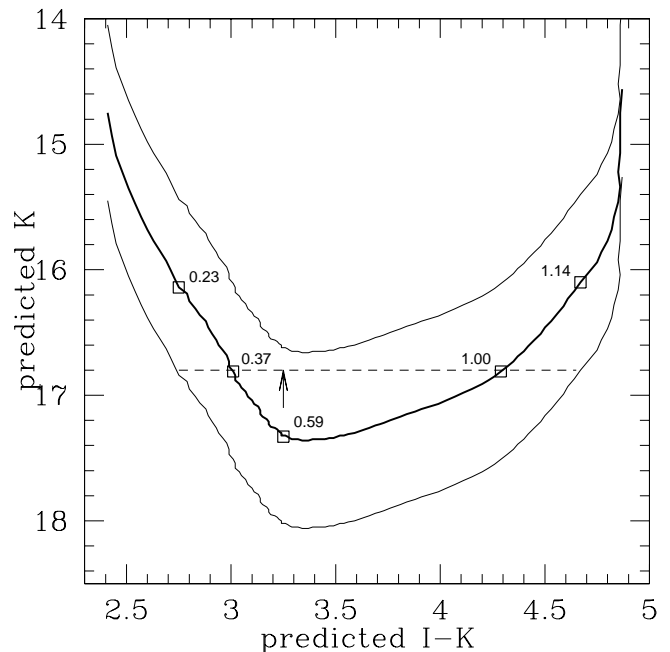
FIG. 5.—Predicted K-band magnitude vs. $I-K$ color for the lensing galaxy (*thick solid line*) for different lensing redshifts. Shown are the 1 σ errors (*thin solid lines*) in the predicted galaxy magnitude, the observed galaxy K magnitude (16.8; *dashed line*), and the $I-K$ color (3.25; *arrow*). Boxes denote lens redshifts of 0.23, 0.37, 0.59, 1.00, and 1.14 from blue to red.

with the two most probable redshift estimates at $z = 0.37$ and $z = 1.00$. A lens redshift as high as 1.00 seems somewhat unlikely, as the implied velocity dispersion is 320 km s^{-1}, corresponding to a 4.5 L_* galaxy; these values are somewhat extreme and are typically found only in the very brightest members of clusters (Pahre, Djorgovski, & de Carvalho 1998). The $I-K$ color of the lens galaxy (using magnitudes measured inside an aperture radius of $1''4$) is 3.25 mag (Fig. 5, *arrow*). This is consistent with a lens redshift of $z \sim 0.6$, based on the above analysis, and also argues for a lens redshift under unity.

4.3. *Lens Model and Differential Time Delay*

We have fitted a simple lens model to the system, which is straightforward to model given the relatively simple image geometry. The small misalignment between the galaxy and the two quasars implies that some asymmetry must be present in the lensing potential. Our basic model uses an SIS potential for the lensing galaxy, plus an external shear to break the circular degeneracy. It has a two-dimensional effective lensing potential ϕ, given by

$$\phi = br - \frac{\gamma}{2} r^2 \cos 2(\theta - \theta_\gamma) . \qquad (2)$$

The major axis of the isopotential lines point along θ_γ, which is also the direction (modulo 180°) of the perturbing mass responsible for the shear. Note that the sign convection for the shear term is the opposite of that adopted by Schechter et al. (1997), whose SIS-plus-shear model predicts a perturbing mass at ±90° from θ_γ. In the limit of vanishing shear ($\gamma \to 0$), the strength of the potential b corresponds to the Einstein radius of the system, which is also half of the observed image separation. There are five model parameters (including two for the unknown quasar source position) and five constraints (the relative positions of components A and B with respect to the lensing galaxy and the A/B flux ratio). Thus, there are no degrees of freedom and our best fit is characterized by $\chi^2 = 0$.

Parameter values were obtained by minimizing residuals in the source plane. For a given parameter set, each quasar image is traced back from the image plane to the source plane using the lens equation, and the optimal model parameters are then found by minimizing residuals between the model source position and the backward projection of the image positions.

To constrain the model, we use the relative astrometry from the *HST* *I*-band data and the A/B flux ratio from the *K*-band PSF model, which ought to be relatively unaffected by microlensing. Our best-fit parameters are presented in Table 5. This model predicts modest magnification factors of 3.12 for component A and 0.88 for component B; thus,

neither component is highly magnified. If the required shear of $\gamma = 0.048$ is due to a neighboring galaxy with the same potential as the main lensing galaxy, it would be located $6''$ away. There are several galaxies within $6''$–$10''$ of the lens, but none of them match the predicted position angle of the external tide. The asymmetry in the lensing potential may also arise from large-scale structure perturbations along the line of sight (Bar-Kana 1996), or it may simply be internal to the lensing galaxy.

The predicted time delay for the system is rather insensitive to the exact choice of Ω_m and Ω_Λ, but it is a sensitive function of the redshift of the lensing galaxy. Adopting a lens redshift in the range of 0.4–0.6, our model predicts a differential time delay of from 19.0 to 36.2 h^{-1} days. Clearly, a spectroscopic redshift is required to predict a precise time-delay.

5. CONCLUSIONS

We have presented optical, IR, and spectral observations of the new lensed quasar CTQ 327, a $1''22$ double of a background $z = 1.37$ quasar. The lensing galaxy is confidently detected after PSF subtraction of the two quasar components, and its well-modeled $r^{1/4}$ profile, together with the absence of strong intervening absorption features in the quasar spectra, suggest an elliptical lensing galaxy. Optical monitoring of the quasar pair shows component A to have brightened by 0.14 mag over 3 months, while component B does not show any significant change over the same period.

A lens redshift in the vicinity of $0.4 < z < 0.6$ is suggested based on *I*- and *K*-band photometry of the lensing galaxy, but values outside this range are not confidently ruled out from the present data. The above redshift range implies differential time delays between quasar images on the order of 1 month, which may prove a challenge to measure unless the quasar is variable on a similarly short timescale.

Spectral differences are observed in the continuum and emission-line properties of the two quasar images. There is evidence of a relatively soft continuum enhancement in component A's spectrum, possibly due to microlensing amplification of component A's continuum by stars in the foreground lensing galaxy, as well as evidence of intrinsic differences in the shapes of the emission profiles between the two components. The latter cannot be explained solely by microlensing of the compact continuum source and may be a result of intrinsic variability of the quasar's broad-line region coupled with the system's differential time delay or of a more complicated microlensing pattern that affects both the continuum and emission-line regions of the source quasar. Future optical monitoring (primarily in the *g*-band) and follow-up spectroscopic observations of the system will help determine the nature of variability observed thus far.

TABLE 5
CTQ 327 LENS MODEL

b (arcsec)	β_x (arcsec)	β_y (arcsec)	γ	θ_γ (deg)
0.623	−0.311	0.0592	0.050	−68.9

NOTE.—Positions are observer coordinates, with west along $+x$ and north along $+y$, and are centered on the lensing galaxy; β_x and β_y mark the source position. The position angle for θ_γ is measured east of north.

REFERENCES

Allen, C. W., & Cox, A. N. 2000, Allen's Astrophysical Quantities (4th ed.; Berlin: Springer)
Bar-Kana, R. 1996, ApJ, 468, 17
Bessel, M. S. 1990, A&AS, 83, 357
Browne, I. W. A., et al. (Class Collaboration). 2001, in ASP Conf. Ser. 237, Gravitational Lensing: Recent Progress and Future Goals, ed. T. Brainerd & C. S. Kochanek (San Francisco: ASP), 15
Claeskens, J.-F., Surdej, J., & Remy, M. 1996, A&A, 305, L9
Coleman, G. D., Wu, C.-C., & Weedman, D. W. 1980, ApJS, 43, 393
Dressler, A., Lynden-Bell, D., Burstein, D., Davies, R. L., Faber, S. M., Terlevich, R., & Wegner, G. 1987, ApJ, 313, 42
Epps, H. W., & Miller, J. S. 1998, Proc. SPIE, 3355, 48
Faber, S. M., & Jackson, R. E. 1976, ApJ, 204, 668
Fruchter, A., & Hook, R. N. 1997, Proc. SPIE, 3164, 120
Fukugita, M., Futamase, T., Kasai, M., & Turner, E. L. 1992, ApJ, 393, 3
Fukugita, M., Ichikawa, T., Gunn, J. E., Doi, M., Shimasaku, K., & Schneider, D. P. 1996, AJ, 111, 1748
Fukugita, M., Shimasaku, K., & Ichikawa, T. 1995, PASP, 107, 945
Gregg, M. D., & Minniti, D. 1997, PASP, 109, 1062
Gregg, M. D., Wisotzki, L. Becker, R. H., Maza, J., Schechter, P. L., White, R. L., Brotherton, M. S., & Winn, J. N. 2000, AJ, 119, 2535
Holtzman, J., et al. 1995, PASP, 107, 1065
Kayser, R., Refsdal, S., & Sabell, R. 1986, A&A, 166, 36
Kimble, R. A., et al. 1997, ApJ, 492, L83
King, L. J., Browne, I. W. A., Marlow, D. R., Patnaik, A. R., & Wilkinson, P. N. 1999, MNRAS, 307, 225
Kochanek, C. S. 1992, ApJ, 384, 1
———. 1996, ApJ, 466, 638
Kochanek, C. S., et al. 2000, ApJ, 543, 131

Krist, J., & Hook, R. 2002, Tiny Tim User's Guide (Baltimore: STScI)
Landolt, A. U. 1992, AJ, 104, 340
Maller, A. H., Simard, L., Guhathakurta, P., Hjorth, J., Jaunsen, A. O., Flores, R., & Primack, J. R. 2000, ApJ, 533, 194
Maoz, D., et al. 1993, ApJ, 409, 28
Matthews, K., & Soifer, B. T. 1994, in Infrared Astronomy with Arrays: the Next Generation, ed. I. McLean (Dordrecht: Kluwer), 239
Maza, J., Ruiz, M. T., González, L. E., Wischnjewsky, M., & Antezana, R. 1993, Rev. Mexicana Astron. Astrofis., 25, 51
Morgan, N. D., Dressler, A., Maza, J., Schechter, P. L., & Winn, J. N. 1999, AJ, 118, 1444
Newberg, H. J., Richards, G. T., Richmond, M., & Fan, X. 1999, ApJS, 123, 377
Pahre, M. A., Djorgovski, S. G., & de Carvalho, R. R. 1998, AJ, 116, 1591
Press, W. H., Teukolsky, S. A., Vetterling, W. T., & Flannery, B. P. 1992, Numerical Recipes in C (Cambridge: Cambridge Univ. Press)
Refsdal, S. 1964, MNRAS, 128, 307
Schechter, P. L., et al. 1997, ApJ, 475, L85
Steidel, C. C., & Sargent, W. L. W. 1991, ApJ, 382, 433
White, R. L., et al. 2000, ApJS, 126, 133
Winn, J. N. 2001, Ph.D. thesis, MIT
Wisotzki, L., Christlieb, N., Bade, N., Beckmann, V., Köhler, T., Vanelle, C., & Reimers, D. 2000, A&A, 358, 77
Wisotzki, L., Köhler, T., Kayser, R., & Reimers, D. 1993, A&A, 278, 15
Wisotzki, L., Köhler, T., Lopez, S., & Reimers, D. 1996, A&A, 315, L405
Witt, H. J., Mao, S., & Schechter, P. L. 1995, ApJ, 443, 18
Woodgate, B. E., et al. 1998, PASP, 110, 1183
York, D. G., et al. 2000, AJ, 120, 1579